Water Research, Volume 228, Part A, 1 January 2023, Article number 119360
DOI: 10.1016/j.watres.2022.119360

A modelling approach to explore the optimum bubble size for micro-nanobubble aeration

Wei Fan[a], Yuhang Li[a], Tao Lyu[b], Jia'ao Yu[a], Zhen Chen[a], Peter Jarvis[b], Yang Huo[a,*], Dan Xiao[c,*], Mingxin Huo[a]

[a]*School of Environment, Northeast Normal University, 2555 Jingyue Street, Changchun 130117, China*

[b]*School of Water, Energy and Environment, Cranfield University, College Road, Cranfield, Bedfordshire MK43 0AL, United Kingdom*

[c]*Jilin Academy of Agricultural Science, 1363 Shengtai Street, Changchun, 130033, China*

Corresponding authors: huoy362@nenu.edu.cn (Y. H.). xiaodan_nky@163.com (D. X.)

Abstract

Bubble aeration has been widely applied in water/wastewater treatment, however its low gas utilization rate results in high energy consumption. Micro-nanobubble (MNB) is an emerging technology that has the potential to significantly increase gas utilisation due to their high relative surface area and high gas-liquid mass transfer efficiency. In this study, we demonstrate through calibrated models that MNB of an optimum bubble size can shrink and burst at or below the water surface enabling 1) all encapsulated gas to thoroughly dissolve in water, and 2) the bursting of nanobubbles to potentially generate free radicals. Through the understanding of MNB dimensional characteristics and bubble behaviour in water, a dynamic model that integrated force balance (i.e. buoyancy force, gravity, drag force, Basset force and virtual mass force), and mass transfer was developed to describe the rising velocity and radius variation of MNB along its upward trajectory. Unlike for conventional millimetre-sized bubbles, intensive gas dissolution of MNBs led to radius reduction for small bubbles, while a large initial radius triggers bubble swelling. The initial water depth was also crucial, where greater depth could drive the potential for bubble shrinkage so that they were more liable to contract. For example, the optimum bubble size of air (42-194 μm) and oxygen (127-470 μm) MNB that could achieve a complete gas transfer (100% gas utilisation) at certain water depths (0.5-10 m) were calculated. The modelling results of microbubble (10-530 μm) were well validated (R^2>0.85) by the experimental data. However, the performance of nanobubble (<1 μm) aeration remained elusive due to a lack of experimental investigations. In this study, the proposed model and results can provide a new insight into understanding the bubble

dynamics in water and provide fundamental guidance for practitioners to upgrade the bubble aeration system.

Keywords: Bubble dynamics; gas-liquid transfer; micro-nanobubble technology; water and wastewater treatment

1. Introduction

Bubble aeration has been widely applied in many areas for water and wastewater treatment, energy production, aquaculture and chemical engineering (Fan et al., 2021; Courtney et al., 2021). Conventional millimetre-sized bubbles aeration offers effective mixing consequent but with limited oxygen transfer efficiency (6-10%), for example in activated sludge treatment plants (Zhang et al., 2020). Bubble size can significantly affect the gas-liquid mass transfer, where small bubbles are more efficient due to the increased gas/liquid contact area and extended bubble residency time in solutions. Therefore, micro-nanobubble (MNB) technology, with a reported oxygen transfer efficiency of 30–100% (Muroyama et al., 2013; Abadie et al., 2022), has recently been developed and utilised in biological, chemical and environmental applications (Azevedo et al., 2016; Temesgen et al., 2017).

During conventional bubble aeration, large bubbles in the water will rise, swell, and collapse at the water surface, which results in low gas-liquid transfer efficiency. On the contrary, MNB may shrink and burst at or below the water surface due to the lower buoyancy and high gas transfer rate. However, the basic definition/categorisation of MNBs remains inconsistent. Takahashi et al. (2007) and Terasaka et al. (2011) labelled microbubbles or fine bubbles as tiny bubbles with sizes in the range of 10-50 or 10-60 μm, respectively. Agarwal et al. (2011) categorized bubbles under the size of 200 nm as nanobubbles. Seddon et al. (2012) reported that bulk nanobubbles were observed in solutions, with typical radii of curvature of 50-100 nm. Zimmerman et al. (2011) defined nanobubbles as bubbles having sizes in the range of 1 nm to 1 μm. In 2017, the published standard of ISO 20480-1:2017 defined a fine bubble (microbubble) as a bubble with a volume equivalent diameter of less than 100 μm and an ultrafine bubble (nanobubble) as a bubble with a diameter of fewer than 1 μm (ISO, 2017). In many cases, researchers lumped the microbubbles and nanobubbles together and called them ‘micro-nano bubbles’ without strict partition. In terms of real implementation,

practitioners need clear guidance in choosing the specific size of MNB for aeration. The application of bubbles with the optimum size can also avoid energy waste caused by the excessive pursuit of the production of ultrafine bubbles.

Besides the characteristics of small bubble size and large specific surface area, MNBs also show various fascinating properties of the negatively charged surface and the capability of generating free radicals to promote pollutant removal (Takahashi et al., 2007). Therefore, MNBs have also been used to remediate hydrocarbon-contaminated soil (Agarwal et al., 2016), reduce surface (membranes) fouling (Ghadimkhani et al., 2016), and remove micropollutants in wastewater (Li et al., 2009). Although the importance of free radical generation from the collapse of micro-nanobubbles has been questioned for the range of size bubbles (1-100 μm) typically seen for most microbubble generators (John et al., 2022a). For smaller bubbles with low nm scale (<200 nm), some studies have either directly monitored or indirectly demonstrated the function through experimental investigations (Tang et al., 2021). Takahashi et al. (2007) proposed a theory based on the accumulation of ions to explain radical generation from collapsing microbubbles. The shrinking of the bubble leads to the accumulation of ions near the interface, resulting in a rapid increase in the absolute value of the ζ potential (Takahashi, 2005). Then, the drastic environmental change caused by the extinction of the gas-water interface triggers radical generation via the dispersion of the elevated chemical potential that has accumulated around the interface (Takahashi, et al., 2012). Yasui et al. (2018b) claimed that the temperature and pressure inside a bubble increased to about 3000 K and 1-5 GPa, respectively, at the final moment of bubble dissolution due to the quasi-adiabatic compression. These extreme conditions thus led to another possible mechanistic route for hydroxyl radical generation. Therefore, delivering an appropriately sized bubble that can shrink at or below the water surface can not only achieve the completed gas utilisation during aeration but also generate activated oxidizers to boost the treatment.

To obtain the perfect bubble size for aeration, it is important to understand the dynamics of the bubble rising in water, including the rising velocity and diameter change. Stoke's law, Davies and Taylor’s equation, or Hadmard-Rybczynski's equation (H-R equation) are the most commonly used models to estimate the terminal velocity of a single sphere bubble at a low Reynolds number (even approaches to zero) (Parkinson et al., 2008; Parmar et al., 2015; Liu

et al., 2016). These readily applied analytic formulas were developed to establish the relationship between the specific diameter of the bubble and the terminal velocity in ideal conditions (uniform motion), thus could not describe the dynamic changes. The Epstein-Plesset theory (Plesset and Satwindar, 1982) and models proposed by Yasui et al. (2018b) and Xue et al. (2022) describe the gas diffusion, heat transfer, and energy transformation over time for a dissolving bubble. However, these models do not consider the bubble rising in the liquid because their focus was on the bubble dynamics at the final dissolution stage when the rising velocity of a bubble with a diameter in the tens of nanometre range could be ignored. Hirai et al. (2015) also proposed a theoretical equation for the change of microbubble diameter, but it was assumed that the change rate was constant during the rising process, which disagreed with the conventional view that the rate of bubble shrinkage increases as bubbles rise (Yasui et al., 2016). Therefore, the development of the theory and an integrated dynamic model are urgently needed to determine the threshold diameter for the best MNB aeration.

The study aims to develop and investigate a numerical model that can identify the optimum bubble size for the MNB aeration for thorough gas transfer and free radicals generation. We claim that only a bubble with a radius smaller than the threshold value can collapse below the water surface and achieve the best MNB aeration (Fig. 1a). The model considered both force balances (buoyancy force, gravity, drag force, Basset force, and virtual mass force) and mass transfer of a gas bubble rising in water. Additionally, the experimental data from the literature were collected to validate the model. Finally, the optimum bubble size of air and oxygen MNB at certain water depths (0.5-10 m) was calculated. The proposed model and results aim to provide a new insight to understand the bubble dynamics in water and fundamental guidance for practitioners to upgrade the bubble aeration system.

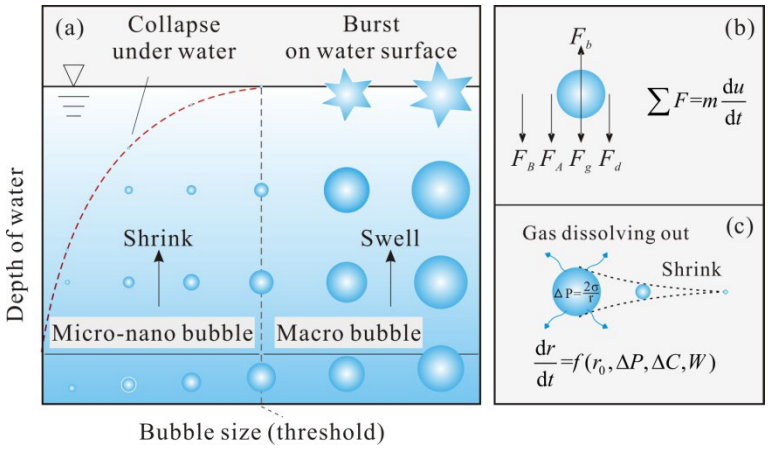

Fig. 1. The framework of the proposed model. (a) Only the bubbles with a radius smaller than the threshold value would collapse below the water surface, dissolve all gas inside the bubble and potentially generate free radicals. (b) The total net force that acts on the bubble determines the velocity and acceleration. (c) The variation of bubble radius depends on the initial radius, the difference in pressure and gas concentration inside and outside the bubble, and mass transfer coefficient.

2. Materials and methods

2.1. Model descriptions

The model framework is shown in Fig. 1 which considers a single isolated gas bubble in water. There are five forces (Fig. 1b) that act on the bubble (Kulkarni and Joshi, 2005; Muhlbauer et al., 2019). The buoyancy (F_b) is an upward force, while the gravity (F_g), drag (F_d), Basset (F_B) and virtual mass (F_A) are the downward forces. Interactions between these forces are determined by gas density (ρ_g), surface tension (σ), viscosity (μ) and initial bubble size producing various effects on the rising trajectories and radius (r) variation. The variations of the inertial and viscous energy dissipation were considered to quantify the drag force. The bubble size and velocity at a specific time during the rising process were calculated as a function of bubble size, gas type and water depth. At a specific flow regime, the radius of the bubble that will shrink and precisely collapse at the water surface was determined as the corresponding threshold value. To simplify the bubble rising process, all analyses are implemented based upon the following commonly used assumptions (Kulkarni and Joshi, 2005; Yasui et al., 2016; Xue et al., 2022): 1) The bubble remains spherical during the rising process; 2) The surrounding water is static; 3) The temperature inside the bubble remains

stable most of the time and only increases to about 3000 K at the final moment (in several picoseconds) of collapse; 4) Gas inside the bubble is ideal; 5) The initial rising velocity equals zero at time t=0 s.

2.1.1. Description of the bubble rising and trajectory

According to Newton's Second Law, the balance of forces can be presented as Eq. (1):

$$m_g \frac{du}{dt} = F_g + F_b + F_d + F_A + F_B \tag{1}$$

where m_g is the mass of the gas bubble; u is the rising velocity of the bubble at a time t. All these forces are given as follows (Kulkarni and Joshi, 2005; Moreno-Casas and Bombardelli, 2016; Muhlbauer et al., 2019)

$$F_g = -\frac{4\pi}{3} r^3 \rho_g g \tag{2}$$

$$F_b = \frac{4\pi}{3} r^3 \rho_l g \tag{3}$$

$$F_d = -\frac{1}{2} \pi r^2 \rho_l u^2 C_D \tag{4}$$

$$F_A = -\frac{4\pi}{3} r^3 \rho_l K_m \frac{du}{dt} \tag{5}$$

$$F_B = -K_B r^2 \sqrt{\pi \rho_l \mu} \int_0^t \frac{du}{d\tau} \cdot \frac{d\tau}{\sqrt{t-\tau}} \tag{6}$$

where ρ_g and ρ_l are the densities of the gas and liquid, respectively; g is the acceleration of gravity; τ is a dummy integration variable; K_m is the virtual mass coefficient and is commonly set to 0.5 (Feng and Bolotnov, 2017); K_B is the Basset coefficient and equal to 6 (Chuang and Hibiki, 2017); C_D is a drag coefficient that is related to the Reynolds number ($Re = \frac{2ur}{\mu}$) and Eotvos number ($E_O = \frac{4r^2 g\left(\rho_l - \rho_g\right)}{\sigma}$), where μ is the viscosity of liquid and σ is the surface tension of the liquid.

The relationship between C_D, E_O and Re is shown in Eq. (7) (Darmana et al., 2009):

$$C_D = \max\left\{\min\left[\frac{16}{Re}\left(1+0.15\,Re^{0.687}\right), \frac{48}{Re}\right], \frac{8}{3}\frac{E_O}{Eo+4}\right\} \quad (7)$$

Combining Eq. (1)- (6), we get Eq. (8) illustrating the acceleration of the bubble:

$$\frac{du}{dt} = \frac{(\rho_l - \rho_g)g}{\rho_g + K_m\rho_l} - \frac{3u^2\rho_l}{8r(\rho_g + K_m\rho_l)}C_D - \frac{3K_B\sqrt{\pi\rho_l\mu_l}}{4\pi r(\rho_g + K_m\rho_l)}\int_0^t \frac{du}{d\tau}\cdot\frac{d\tau}{\sqrt{t-\tau}} \quad (8)$$

The bubble trajectory is thus predicted by solving Eq. (9):

$$\frac{dz}{dt} = u \quad (9)$$

where z is water depth (the distance from the bubble centre to the water surface).

2.1.2. Description of the variation of bubble size

While a bubble rises in the liquid, the gas in the bubble keeps dissolving during this process. The bubble size (radius) is a function of inner pressure, liquid pressure (depth under the water surface), surface tension and gas diffusion at the gas-liquid interface. Considering that the gas in the bubble is an ideal gas, the ideal gas state equation is applicable as follows:

$$V\frac{dP}{dt} + P\frac{dV}{dt} = \frac{PV}{n}\cdot\frac{dn}{dt} \quad (10)$$

Then the time derivative of the bubble radius can be expressed in Eq. (11):

$$\frac{dr}{dt} = \frac{r}{3}\left(\frac{1}{n}\frac{dn}{dt} - \frac{1}{P}\frac{dP}{dt}\right) \quad (11)$$

where V is the volume of the bubble; n is the total number of moles of the gas inside the bubble; P is the internal pressure of the bubble, and can be described by the Young-Laplace equation, $P = P_0 + \rho_l g z + \frac{2\sigma}{r}$, where P_0 is the atmospheric pressure.

Therefore, the variation of P can be calculated as follow:

$$\frac{dP}{dt} = \rho_l g u - \frac{2\sigma}{r^2}\cdot\frac{dr}{dt} \quad (12)$$

For an individual bubble, the gas diffusion at the gas-liquid interface can be described in Eq. (13):

$$\frac{dn_i}{dt} = 4\pi r^2 W_i (C_{a,i} - C_{s,i}) \quad (13)$$

where n_i is the number of moles inside a bubble for the gas species i (i. e. nitrogen and

187 oxygen in the air); W_i is the mass transfer coefficient at the bubble surface for the gas
188 species i; $C_{a,i}$ is the concentration of the dissolved gas species i in the surrounding
189 fluid; $C_{s,i}$ is the concentration of the dissolved gas species i on the bubble skin.

190 The mass transfer coefficient W_i is considered to depend on the gas-to-liquid diffusivity,
191 density, viscosity as well as how the transfer of gas from the bubble takes place (Miner et al.,
192 1986). Accordingly, the mass transfer coefficients, W_i are given by (Miner et al., 1986):

193
$$W_i = \begin{cases} 2\sqrt{\dfrac{D_i u}{2\pi r}} & r > 0.15 \text{ cm} \\ 7.53 r \sqrt{84.17 D_i} & 0.03 < r \le 0.15 \text{ cm} \\ 0.31 \left(\dfrac{\mu g}{\rho_l}\right)^{1/3} \left(\dfrac{\mu}{\rho_l D_i}\right)^{-2/3} & r \le 0.03 \text{ cm} \end{cases} \quad (14)$$

194 where D_i is the molecular diffusivity of the gas species i ($D_{N_2} = 1.90 \times 10^{-9}$ m^2/s ,
195 $D_{O_2} = 2.50 \times 10^{-9}$ m^2/s).

196 The concentration of the dissolved gas species i on the bubble skin $C_{s,i}$ is calculated by
197 Henry's law constant (Yasui et al., 2016):

198
$$C_{s,i} = \frac{10^3 \rho_l r_{s,i} P}{K_{H,i} M_{\mathrm{H_2O}}} \quad (15)$$

199 where $K_{H,i}$ is Henry's law constant of the gas species i at the bubble wall; $M_{\mathrm{H_2O}}$ is the
200 molecular weight of H_2O (=18 g/mol); $r_{s,i}$ is the molar ratio of the gas species i inside the
201 bubble, $r_{s,i} = n_i / n_t$, n_i is the instantaneous number of moles of the gas species i and n_t
202 is the total number of moles inside a bubble ($n_t = n_{O_2} + n_{N_2}$).

203 Thus, during the bubble rising process, the oxygen utilization coefficient j_{O_2} can be
204 calculated by the following equation:

205
$$j_{O_2} = \frac{n_{O_2,0} - n_{O_2,t}}{n_{O_2,0}} \quad (16)$$

206 where $n_{O_2,0}$ is the initial number of moles of oxygen inside the bubble; $n_{O_2,t}$ is the number

of moles of oxygen inside the bubble at time *t*.

$K_{H,i}$ is a function of temperature and can be calculated using the following equations (Yasui et al., 2016):

$$\ln\left(\frac{K_{H,\mathrm{N_2}}}{10^9}\right) = 58.190472 - \frac{86.32129}{T/100} - 24.79808\ln\frac{T}{100} \tag{17}$$

$$\ln\left(\frac{K_{H,\mathrm{O_2}}}{10^9}\right) = 55.017904 - \frac{83.91236}{T/100} - 23.24323\ln\frac{T}{100} \tag{18}$$

where T is the temperature in Kelvin.

The concentration of the dissolved gas species i in the surrounding ambient fluid $C_{a,i}$ is calculated by Eq. (18)

$$C_{a,i} = \frac{10^3 \rho_l P_0}{K_{H,i} M_{\mathrm{H_2O}}} r_i \tag{19}$$

where r_i is the molar ratio of the gas species i in the air ($r_{N_2} = 0.79$, $r_{O_2} = 0.21$).

Substituting Eq. (12) ~ (19) into Eq. (11), the final form of the derivative of bubble radius can be obtained in Eq. (20):

$$\frac{dr}{dt} = \frac{3RTr\sum W_i(C_{a,i} - C_{s,i}) + \rho_l g u r^2}{3rP_0 + 3r\rho_l gz + 4\sigma} \tag{20}$$

where R is the universal gas constant ($8.31\ Pa\cdot m^3/(mol\cdot K)$). Therefore, the velocity, trajectory and radius of the bubble at time *t* can be found from Eq. (8), (9) and (20).

2.2. Model calculations

The proposed model was programmed and computed by MATLAB 2020a. By inputting different parameters, such as water depth, initial bubble radius, gas type and liquid density, the bubble motion data under different scenarios are obtained, such as radius change, velocity and trajectory.

2.2.1 Calculation of Basset force

The Basset force, also called 'history force', is a kind of viscous force, which arises due to the

lagging boundary layer development with changing relative velocity (acceleration) of bodies (particles or bubbles) moving through a fluid (Barrio-Perotti et al., 2009; Moreno-Casas and Bombardelli, 2016). In this study, the size of the bubble is changing during bubble rising and the forces exerting on the bubble are not constant, thus the bubble velocity is variable, and the influence of Basset force should be considered. The integral of Basset force in Eq. (6) is a singular integral, and the integrand contains an unknown function to be solved. This feature and the nonlinearity of the equation make the theoretical analysis of differential equations more difficult (Daitche, 2013). Because the integrand in the Basset force expression has a singularity in the integration interval, it belongs to the generalized integral. According to the compound gradient formula, the calculation format for constructing the Basset force integral term is (Text S1 in supporting information shows the proof of Eq. 21):

$$\int_0^t \frac{du}{d\tau}\cdot\frac{d\tau}{\sqrt{t-\tau}} = \frac{1}{2}h\left[\frac{f(0)}{\sqrt{t}} + 2\sum_{i=1}^{n-2}\frac{f(ih)}{\sqrt{t-ih}} + \frac{f(t-h)}{\sqrt{h}}\right] + [f(t)+f(t-h)]\sqrt{h} \quad (21)$$

where $h = t/n$ is the integration step length, and its size is determined by the given calculation accuracy; $f(ih) = \left(\frac{du}{dt}\right)_{t=ih}$ is the acceleration at time ih.

Although the Basset force has been converted to a cumulative form, the model is still a hidden function containing the acceleration term, which is difficult to solve its analytical solution. This study employs a fourth-order Runge-Kutta method (Moreno-Casas and Bombardelli, 2016) to compute the numerical solution of the model. As a single-step method, fourth-order Runge-Kutta has high calculation accuracy, however, each step of this method needs to calculate four slopes of each differential equation and has a large amount of calculation. Thus, the multistep fourth order predictor-corrector (Adams-Bashforth-Moulton) method (Chang and Yen, 1998) is used as an alternative during the middle period of the calculation to ensure the accuracy of the differential equation and reduce the calculation time. Numerical iteration and concrete computational process are discussed in Text S2.

2.2.2 Calculation of the threshold of bubble radius

The tendency of bubble expansion or shrinkage is determined by Eq. (20). Eq. (20) can be rewritten as the sum of Eq. (22) and Eq. (23)

$$f(c)=\frac{3RTr\sum W_i(C_{a,i}-C_{s,i})}{3rP_0+3r\rho_l gz+4\sigma} \tag{22}$$

$$g(r)=\frac{\rho_l gur^2}{3rP_0+3r\rho_l gz+4\sigma} \tag{23}$$

where Eq. (22) indicates the influence of gas dissolution and Eq. (23) indicates the influence of bubble velocity. $f(c)$ is negative because the concretion of dissolved gas in the bubble skin is more than that in the surrounding ambient fluid, while $g(r)$ is positive. In other words, $f(c)$ causes the bubble to shrink while $g(r)$ leads the bubble to expand. If $f(c)>g(r)$, the bubble will shrink; otherwise, the bubble will swell and burst at the water surface.

However, not all shrinking bubbles can collapse exactly at the water surface. The residence time of a bubble in water is controlled by two factors. One is the time that it takes for the bubble to move to the water surface (t_{m}), and the other is the time required for the radius to change to zero (t_{s}). The former is influenced by Eq. (8), while the latter is impacted by Eq. (20). When a bubble precisely collapses at the water surface, the time from Eq. (8) should equal the time gained from Eq. (20). Put another way, when the initial radius is the threshold (r_{c}), the bubble precisely rises to the water surface at the moment the bubble collapses. If the initial radius is less than this threshold, the bubble will collapse under the water surface and potentially generate free radicals, whereas when the initial radius is more than the threshold, the bubble may still shrink but burst at the water surface. This threshold can thus be solved using an iterative method based on the comparison between t_{m} and t_{s}.

2.3. Model validation and optimum bubble size calculation

The bubble motion in the gas-liquid system has been explored extensively at lab scale (Duineveld, 1995; Parkinson et al. 2008; Azevedo et al., 2016; Pawliszak et al. 2019; Tanaka et al. 2020). Therefore, existing experimental data were collected to validate the proposed model. The results of the model were compared with available experimental data from these previous studies, including the terminal velocity, bubble size, and trajectory of bubbles with different initial radii (10-530 μm, see section 3.4). After validation, the model was applied to

290 analyse the bubble dynamics, mass transfer, and determine the threshold of bubble radius
291 for MNB considering various factors (i.e. initial bubble radius, water depth and filled gas). The
292 range of initial bubble radius was from 0 to 1 mm, the range of water depth was from 0.5 to
293 10 m, and two bubble types (air bubble and oxygen bubble) were considered in the model.
294 The liquid phase was pure water.

295 3. Results and discussion

296 3.1. Force balance and bubble motion in water

297 The five forces, i.e. F_b, F_g, F_d, F_B, F_A, and the bubble motion characteristics were
298 calculated from Eq. (2-8) and presented in Fig. 2. During the rising process, the gravitational
299 force was two orders of magnitude lower than the other forces and thus can be neglected,
300 while the buoyancy force was nearly constant for both two bubble sizes (20 and 200 μm) at
301 the selected water depth of 0.5 m. The virtual mass force was proportional to the bubble
302 acceleration du/dt and so its maximum value was at the beginning of the motion and
303 declined to zero as the $du/dt \to 0$. The drag force reached its final value as a result of the
304 increased velocity. The Basset force initially increased and then decreased to zero as the
305 $du/dt \to 0$. During the first moments of the bubble motion, the drag force was small due to
306 the low velocity, where the virtual mass force and the Basset force act against the buoyancy
307 force. When the bubble reaches terminal velocity, the virtual mass vanishes, and the Basset
308 force remains constant at less than 1% of the buoyancy force. At this moment, the buoyancy
309 force mainly overcomes the drag force, and they collectively dominate the bubble movement.
310 For the larger bubble (200 μm), all forces are three orders of magnitude higher than that of
311 the smaller bubble (20 μm), thus the net force exerted on the larger bubble is greater and
312 the larger bubble moves upwards with a higher velocity. Moreover, the time required to
313 reach the final velocity (15-20 ms) far exceeds the time (< 1 ms) required by a smaller bubble
314 (20 μm).

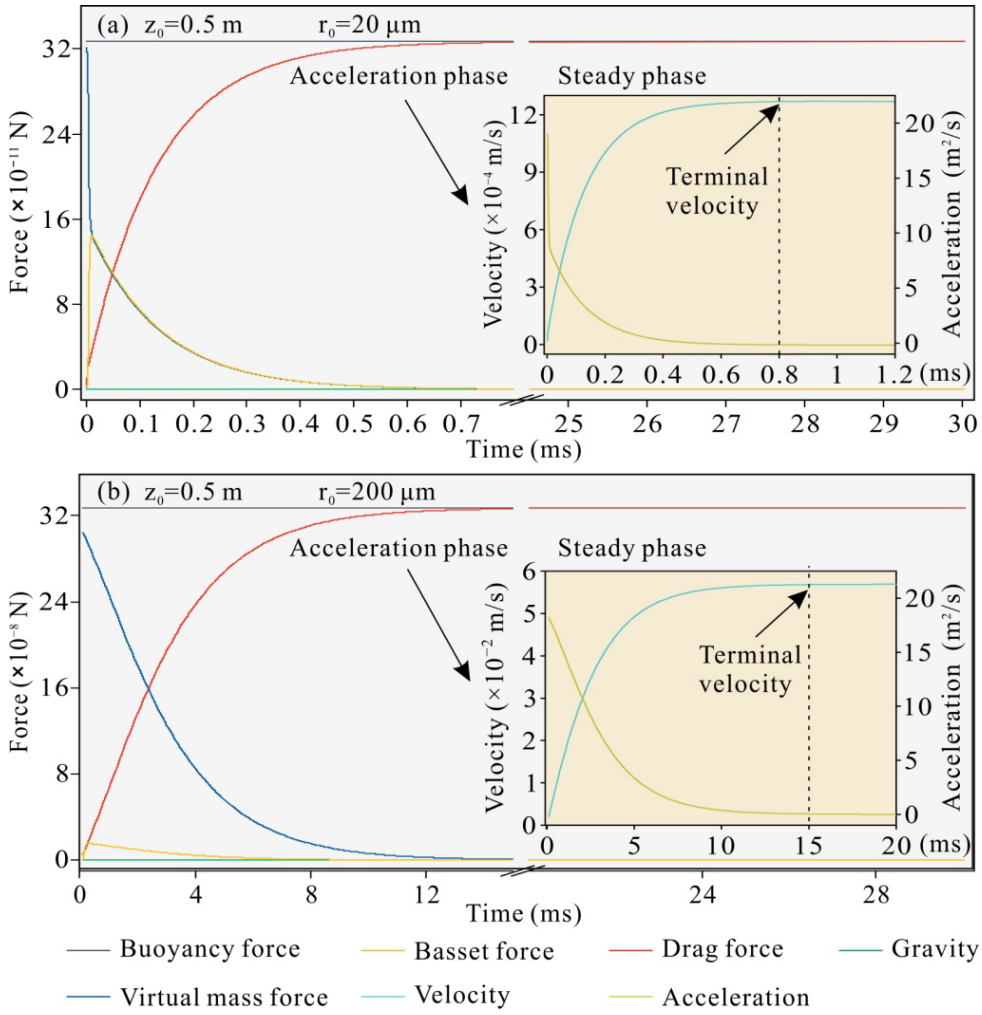

Fig. 2. The hydrodynamic forces and bubble motion characteristics (velocity and acceleration) during rising process for air bubbles at initial water depth of 0.50 m. Two initial radiuses of the bubble were considered at 20 μm (a) and 200 μm (b).

3.2. The dynamics of bubble radius, gas dissolution and inner pressure

Whether the bubble expands or shrinks during the rising process depends on the values of functions described by Eq. (22) and Eq. (23). The bubble sizes of 20 and 200 μm at a water depth of 0.5 m were selected to present the modelling results. For the bubble with the initial radius of 20 μm, it shrinks and totally collapses in water after 54 s (Fig. 3a). The absolute value of $f(c)$ is 2-3 orders of magnitude higher than $g(r)$, indicating that gas dissolution has a greater impact on bubble radius (Fig. 3b). According to Eq. (23), $g(r)$ is proportional to r^2 and thus is more sensitive to initial radius compared with $f(c)$. When the initial radius increases from 20 to 200 μm, the value of $g(r)$ increases by three orders of magnitude whereas $f(c)$ maintains the same order of magnitude (Fig. 3e). In this case, the

$g(r)$ dominates causing the bubble to expand. These results infer that the gas dissolution results in radius reduction for small bubbles, while a large initial radius triggers bubble swelling.

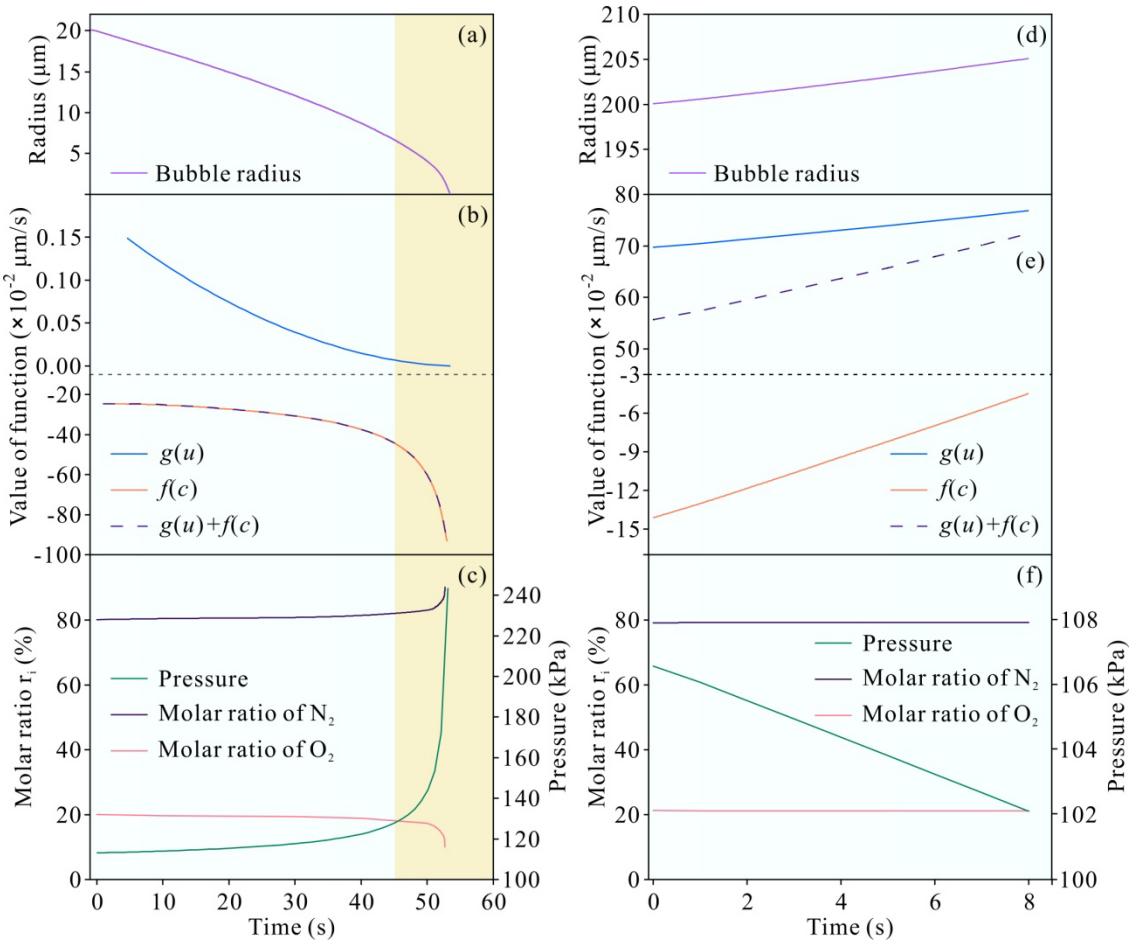

Fig. 3. Changes in bubble radius, the values of functions described by Eq. (20) and Eq. (21), the molar ratios of different gas components (N_2 and O_2) and the inner pressure of the bubble. (a)-(c): the small bubble with an initial radius of 20 μm. (d)-(f): the big bubble with an initial radius of 200 μm. The water depths for all scenarios are 0.5 m.

The dissolution of N_2 and O_2 plays an essential role in radius variation during the bubble rising process. In the present model, the mass transfer coefficient W_i is a function of viscosity, gas molecular diffusivity and gas density. The W_i of each gas species were calculated according to Eq. (14), with values of 1.02×10^{-4} m/s for N_2 and 1.22×10^{-4} m/s for O_2. O_2 has higher solubility than N_2 and hence dissolved into the water faster. For a small bubble with an initial radius of 20 μm, the molar ratio of N_2 inside the bubble almost remains constant in the early stage (about 0.79) and then increases sharply at the final stage (about

0.90 at t=53 s), while the ratio of O_2 decreases from 0.21 to 0.10 (Fig. 3c). This result was consistent with previous research. For example, Yasui et al. (2016) suggested that only nitrogen molecules are present in the shrinking bubble in the final few nanoseconds. The bubble size changed along its rising path in response to both the mass transfer and the local hydrostatic pressure. The rate of change in the bubble radius was constant to begin with (-0.246 μm/s) but increased rapidly to -0.728 μm/s by the end (Fig. 3b). With decreasing bubble size, the specific surface area and pressure inside the bubble increases, thus the partial pressure of the dissolved gas component (the driving force for dissolution) increases and the gas dissolves easily.

The results also indicate that the collapse of these shrinking bubbles creates a localised point which has an extremely high pressure (Fig. 3c). The inner pressure increased from 101.33 kPa to 250 kPa in 55 seconds, and then entered a sharp rising phase. As a consequence, ambient water molecules may be decomposed by shock wave emission to form reactive hydroxyl radicals (Agarwal et al., 2011; Tsuchida et al., 2022). This is of significance in the field of water and wastewater treatment as radicals with a high oxidising power are desired in decontamination or sterilization. For a larger bubble with an initial radius of 200 μm, it rises in water rapidly and expands with decreasing pressure. By this time, the molar ratios of N_2 and O_2 inside the bubble have changed slightly (less than 1%) (Fig. 3f). This is because the inner pressure and $C_{s,i}$ of a big bubble is lower than that of a smaller bubble. In particular, the inner pressure of a small bubble is extremely high at the final stage due to the bubble shrinking, while it is close to atmospheric pressure for the expanded big bubble. Consequently, the gas diffusion at the gas-liquid interface for a big bubble was quite slow and the molar ratio (or concentration) of both gas species inside the bubble have only changed slightly.

3.3. Uncertainties of the performances of nanobubbles

The results show that small bubbles are prone to shrink and disappear in water due to the gas dissolution driven by the pressure difference (Figure 3). The high internal pressure and thermodynamic instability of ultrafine bubbles has been shown in many previous studies (Ohgaki et al., 2010; Lee et al., 2021; Xue et al., 2022). Nevertheless, the longevity of

nanobubbles has also been reported in various experimental observations and their life has been reported to be days to months (Liu et al., 2013; Nirmalkar et al., 2018; Jadhav et al., 2021). This stability has been attributed to several possible mechanisms such as electrostatic repulsion, ion shielding, organic coatings, particle armouring, local oversaturation, and high internal density (Alheshibri et al., 2021; Soyluoglu et al., 2021; Sun et al., 2022). However, each mechanism can only explain part of the phenomena observed and may be inconsistent with many other phenomena. The dynamics of bulk nanobubbles thus remains partly unknown because of the limited development of detection tools for measuring these bubbles and the relevant theory for bubble properties at the nanoscale.

In the present study, the modelling results showed that a bubble with an initial radius of 20 µm shrank to become a 1 µm bubble after 53.07 seconds. By this time, more than 99.90% of oxygen had dissolved from the bubble and the rising velocity was quite slow (less than 3 µm per second). The time for the complete dissolution of oxygen from the 20-µm bubble (Fig. 3a) was 53.61 seconds. These results were in line with previous numerical simulations showing that the radius of any bubble passes the nanoscale during the complete dissolution of the bubble (Yasui et al., 2016; Xue et al., 2022). Though our result does not match the reported long lifetime of bulk nanobubbles, the model prediction is mainly intended to unravel the aeration and dissolution behaviour of MNBs in the middle and early period of aeration, especially when the initial bubble radius in engineering practice is usually in a range of tens to hundreds of micrometres. The period of bubble shrinking in the last tens or hundreds of microseconds has neither been proven or explained quantitatively and thus remains a problem in our understanding of bulk nanobubble behaviour (Yasui et al., 2018a; Sun et al., 2022).

3.4. Model validation

The proposed model was verified using experimental data from previous studies (Table 1). In these previous works, a single air bubble was usually created in distilled water and the bubble behaviour was recorded by a high-speed camera to measure the rising velocity and radius of the bubble. All experiments have been carried out at constant temperature conditions. The predictions from the model presented here were compared with the experimental data using the same conditions. The terminal velocity, bubble size, and

trajectory of bubbles with different initial radii were compared. The comparisons between the predicted results from our model and the experimental measurements are shown in Fig. 4. All theoretical predictions were very close to the experimental data (R^2>0.85). It can be seen that the model was validated over a wide range of bubbling parameters (i. e. the initial radius ranges from 10 to 530 μm) and hence it can provide a good prediction of bubble size, trajectory and rising velocity for many different conditions. There was a small discrepancy for large bubbles (initial radius> 500μm in Fig. 4b). Here the theoretical overestimation can be attributed to the uncertainty in the bubble shape (i. e. deformation) since the experimental bubble size was calculated using a bubble contour method in this study (Duineveld, 1995). Notably, due to the lack of experimental data available for nanobubbles and the unsolved mechanisms (section 3.3), the modelling results for nanoscale bubbles requires further validation.

Table 1

Various operating parameters of the experimental bubble systems used to validate the model proposed in this research.

References	Liquid	Depth of liquid (m)	Gas type	Initial radius (μm)	Temperature
Parkinson et al (2008)	Pure water	0.40	N_2	10-60	22.5 ± 1.5 ℃
Duineveld (1995)	Pure water	0.50	Air	330-530	19.6 ± 0.2 ℃
Tanaka et al (2020)	Pure water	0.50	Air	20	25 ± 1 ℃
Pawliszak et al (2019)	Pure water	0.15	Air	167.5	22 ± 1 ℃

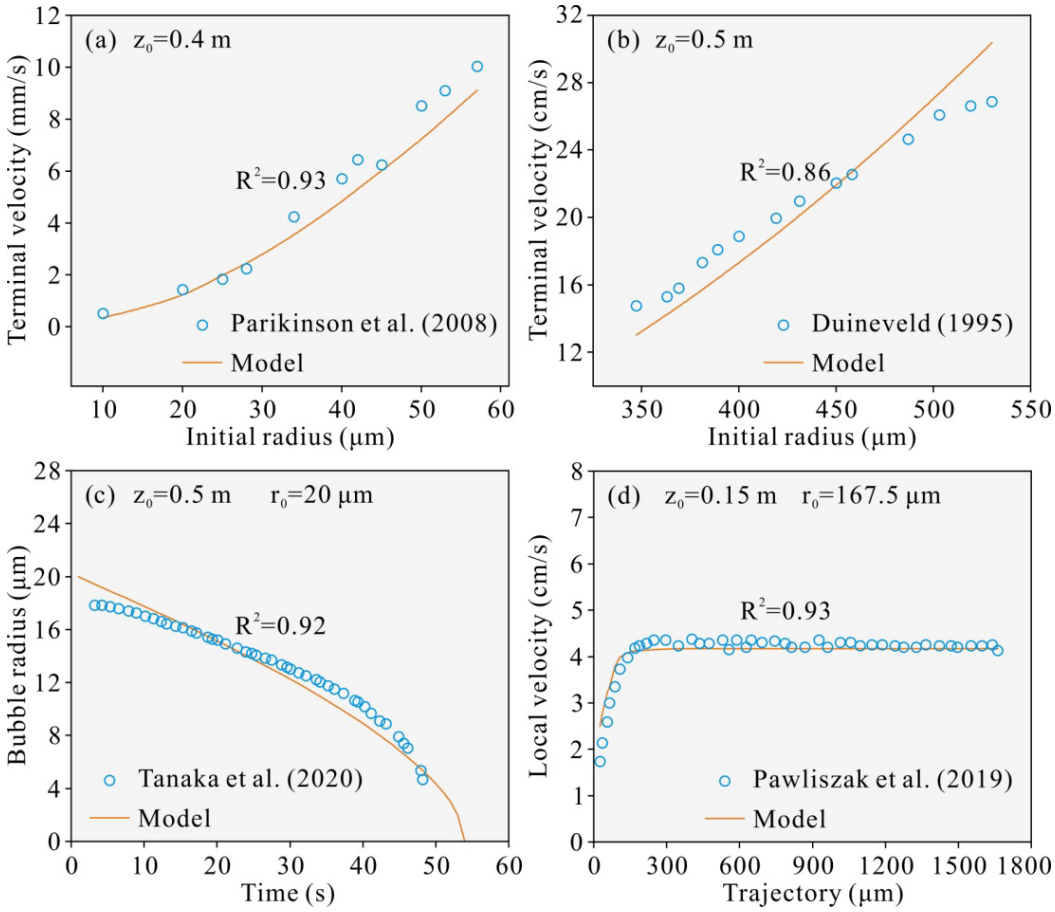

Fig. 4. Comparisons between experimental data and modelling results. Terminal velocity of bubbles with different initial radius 10-60 μm (a) and 350-530 μm (b); (c) Change of bubble radius during rising process, therein water depth is 0.5 m and initial radius is 20 μm; (d) Bubble trajectory and local velocity, therein the initial water depth is 0.15 m and the initial radius is 167.5 μm. Terminal velocity denotes the velocity at the final stage of bubble rising, at this moment the variation of rising velocity in 1 s is less than 1%.

3.5. Determination of the threshold of bubble radius

Based upon the above analysis, we know that the change in bubble radius ($\frac{dr}{dt}$) depends on the balance between negative $f(c)$ and positive $g(r)$ forces which are influenced by the initial bubble size, the external pressure (water depth), and the encapsulated gas type. Fig. 5 a-d shows the modelling results of the size changes along the rising path for air bubbles with different initial radii (20- 400 μm) at specific initial water depths (0.5- 10 m). It clearly shows that there exists a critical bubble radius for each scenario, below which the bubble will shrink, and above which the bubble will grow. The critical bubble radiuses are around 20-50, 50-100, 100-150, and 150-200 μm, when it rises from 0.5, 1.0, 5.0, and 10.0 m deep water,

respectively. That is because greater initial water depth leads to a more negative $f(c)$ and a less positive $g(r)$, which makes the bubble contract more intensively.

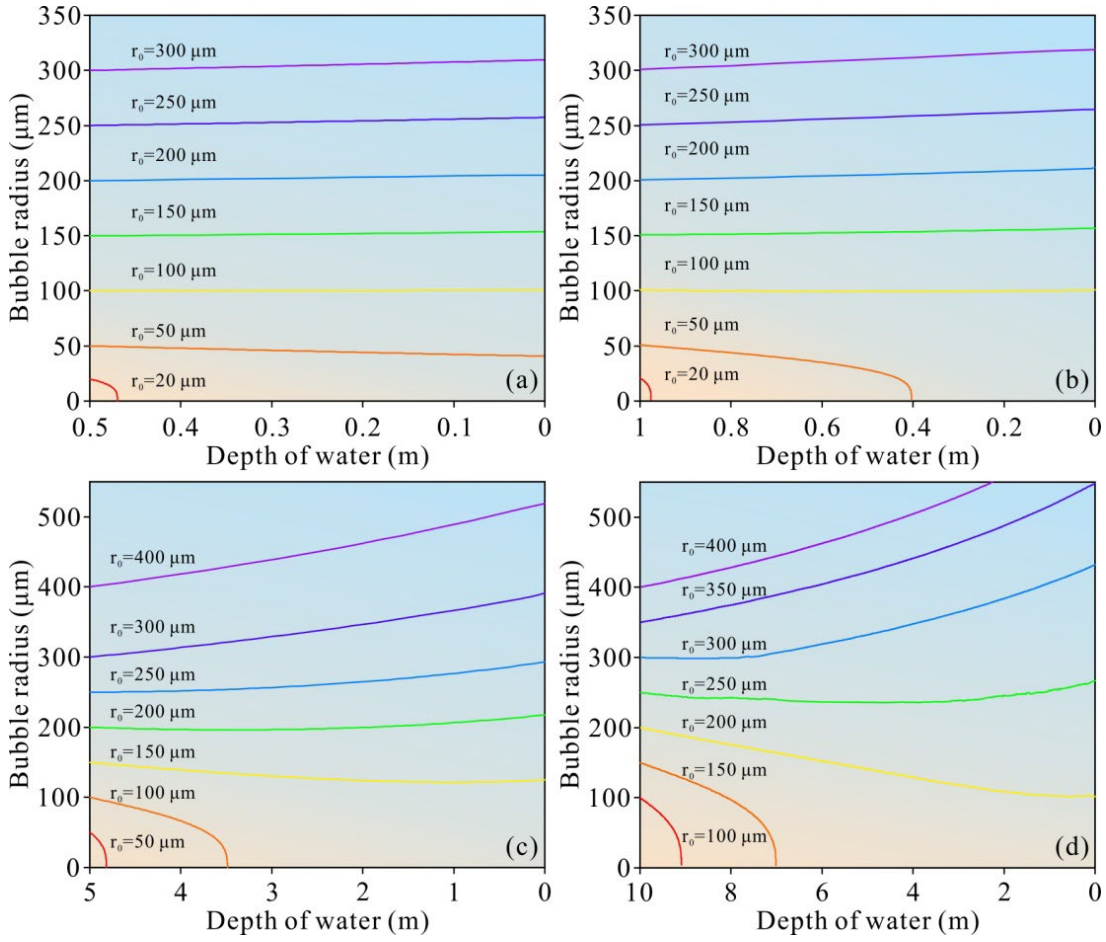

Fig. 5. The variation of radius along the rising path for air bubbles with different initial radii (50-400 μm) at specific initial water depths. The initial water depth is set as 0.5 m (a), 1 m (b), 5m (c), and 10 m (d).

For example, the $f(c)$ for a 200 μm bubble at 10 m water depth was about 4.82 times that at 1 m water depth, while the $g(r)$ for the former was only half of that for the latter (Fig. 6a). In other words, for a given bubble, it may swell in shallow water but contract in deep water. For example, when a bubble with a radius of 127 μm rises from different water depths, we can see that at 0.5 m water depth it will grow quickly in 15.5 s, grow slowly at 1.0 m (in 30.9 s), shrink slowly at 3.0 m in 103.1 s, precisely collapse at the water surface at 5 m in 369.1 s, and shrink quickly at 10.0 m in 194.0 s (Fig. 6b). Greater initial water depth thus drives the potential for high bubble shrinkage, and then raises the threshold of the critical bubble radius.

The oxygen utilization coefficient j_{O_2} for bubbles with different initial radii (1-1000 μm) at different initial water depths (0.5-10 m) was modelled from Eq. (13) and Eq. (16) (Fig. 6c and 6d). For a specific water depth, while the bubble radius was smaller than a certain threshold, the coefficient j_{O_2} always equals 100%. For example, the inflection point (threshold) of the curve in Fig. 6c was 194 μm for initial water depth 10 m. A coefficient value of 100% means that the bubble has collapsed underwater and all the encapsulated gas inside the bubble has thoroughly dissolved in water achieving a complete phase transfer. As the bubble size becomes greater than the threshold, the j_{O_2} decreases with increasing radius and the greater the initial water depth is, the higher the j_{O_2} becomes for and given specific bubble size.

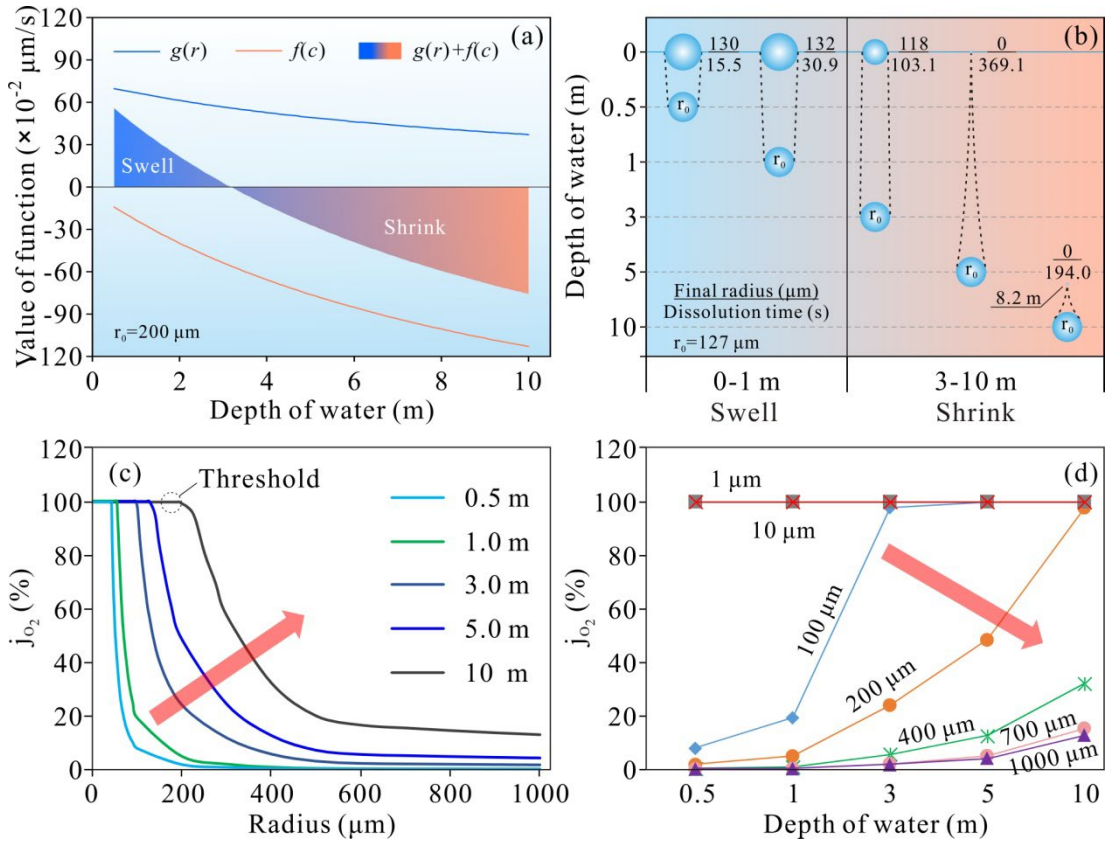

Fig. 6. (a) The shrink and swell potential for a 200 μm bubble at different initial water depths (0.5-10 m). (b) The final radius and position, and dissolution time for a 127 μm bubble at different initial water depths (0.5-10 m). (c) and (d) The oxygen utilization coefficient j_{O_2} for bubbles with different initial radii (1-1000 μm) at different initial water depths (0.5-10 m).

The above results demonstrate the radius variation tendency of the rising bubble. However, the exact threshold of the bubble radius for each scenario has not yet been obtained. A bubble that shrinks and precisely collapses at, or just below, the water surface ($t_m = t_s$) is the desired MNB in the present study. Based on the criteria, the thresholds of bubble radius for two gas species (O_2 and N_2) were determined (Fig. 7a). For air bubbles, the thresholds were 42, 54, 96, 127, 157, and 194 μm for initial water depths of 0.5, 1.0, 5.0, and 10.0 m, respectively. For oxygen bubbles, the equivalent thresholds were 127, 164, 254, 350, 405, and 470 μm. The latter was about 58.72-67.07% higher than the former because the relatively higher solubility of O_2 shortened the t_s compared with N_2. For a water depth of 1m, an air bubble with a radius of 54 μm will shrink and precisely collapse at the water surface in 253.2 s. However, an oxygen bubble under the same condition will totally dissolve under water within 13.1 s and finally collapse at a water depth of 0.96 m. This collapse depth increases with increasing initial bubble size while the residence (shrinkage) time also displays a synchronously increasing tendency. The threshold for an oxygen bubble radius for the same water depth (1 m) was as high as 164 μm. Therefore, the more soluble the gas species, the larger the critical bubble radius will be.

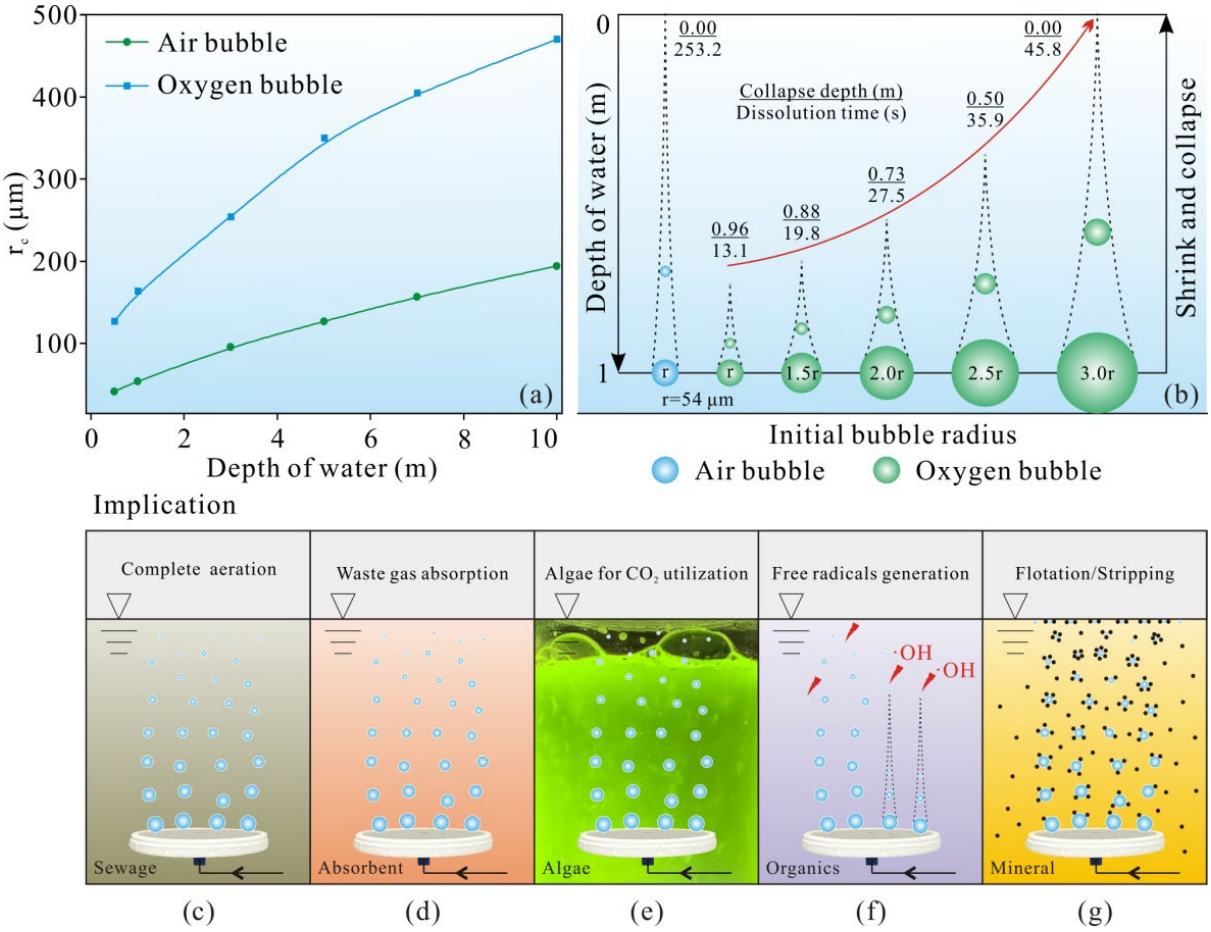

Fig. 7. The threshold values for the critical bubble radius at different initial depths were calculated. The bubbles whose radii are no more than the threshold values can collapse below the water surface, and they are the desired bubbles for complete gas transfer and free radical generation.

3.6. Bubble size selection and further implications

Artificial bubbles are usually formed by dispersing the gas phase into the liquid phase in many different fields such as wastewater treatment, waste gas capture, biomass energy production, froth flotation, and stripping (Lyu et al., 2019; Fan et al., 2021; Liu et al., 2021). Mass transfer and reaction at the two-phase interface are heavily dependent on the bubble size. There are always two main obstacles in these systems. Firstly, large bubbles can quickly rise to the surface and escape from the bulk solution, so gas transfer to the liquid is limited, and the interfacial reaction is incomplete (Levitsky et al., 2022). Secondly, while many studies have paid close attention to the generation of MNBs due to their fascinating characteristics (Fan et al., 2021; John et al., 2022b), the generation of these MNBs is usually associated with high energy consumption (Zimmerman et al., 2011). Therefore, both generation of coarse bubbles and the excessive pursuit of going to smaller bubble scales is not an economic path.

However, there is reason to believe that many bubbling systems are not optimally designed and operated in order to obtain the desired bubble size. As has been demonstrated in the present study, the desired bubble size is case-dependent, which needs to account for the water depth and gas species. An energy-conscious strategy should be adopted whereby bubble contactors are designed such that they generate bubbles that have a slightly smaller diameter than the critical threshold size. In such cases, oxygen will thoroughly dissolve in the liquid to realize complete aeration (Fig. 7c) and the waste gas absorption will be more intensive and there will be no waste gas escape from the reactor (Fig. 7d). In addition, MNBs will dissolve CO_2 faster and therefore increase algal growth for biofuels production (Fig. 7e) and the violent MNBs collapse leads to free radical generation which can be of significance for oxidation of a range of pollutants in water (Fig. 7f). Sufficiently small bubbles also display strong adhesion to mineral particles which can be useful for flotation and stripping (Fig. 7g).

In the present study, we shed light on the hypothesis that the size of desired MNB for aeration can be determined by dimensional characteristics and bubble dynamics in a liquid medium. We proposed the radius thresholds of MNBs for specific water depths, and we expect that this will be a reference for bubbling system design and provide a framework for defining appropriate MNB characteristics. However, despite a number of recent studies, bulk MNBs are still an emerging field and speculation remains prevalent about their existence, stability, and mobility. In addition, both the conceptual and numerical models presented in this study have been simplified to improve their computability and practicability based upon a series of assumptions. Given the complexity of bubble motion in real water bodies or other liquid mediums, further study of the impacts of actual conditions on the radius thresholds is needed. The MNB dynamics may be influenced by coexisting dissolved organic matter, suspended particles (solid impurity), surfactant, gas supersaturation in surrounding liquid and the electrokinetic characterization of these substances. It is possible that the radius thresholds of MNBs in these cases would be different. Nevertheless, they are not discussed here since it would require more targeted research of its own.

4. Conclusions

The present study developed a model with revealed mechanisms for identifying the

optimum bubble size for MNB aeration through effective gas transfer and potential free radical generation. We proposed a smart bubbling strategy herein by generating bubbles with an optimum size: only bubbles with a radius smaller than the threshold value can collapse below the water surface and fulfil the purpose of the best MNB aeration. These targeted MNBs will thoroughly dissolve in water to achieve a complete gas transfer and potentially generate free radicals following bubble collapse to purify the surrounding water. A numerical model was successfully developed to describe the bubble motion and mass transfer during the rising process. The critical thresholds were 54 μm and 194 μm for air bubbles at initial water depths of 1.0 m and 10.0 m, respectively. The two corresponding thresholds for oxygen bubbles were 164 μm and 470 μm. Great initial water depth and soluble gas species drove the high shrinkage potential of bubbles such that the bubbles were more liable to contract. Overall, this study opens up a new prospect on the definition of MNB and provides useful guidance for bubbling system design to realize precise aeration using optimal bubble size.

Credit authorship contribution statement

Wei Fan: Methodology, Investigation, Writing-Original Draft. Yuhang Li: Methodology, Investigation. Tao Lyu: Writing-Review & Editing. Jia'ao Yu: Investigation, Formal analysis. Zhen Chen: Formal analysis. Peter Jarvis: Writing-Review & Editing. Yang Huo: Writing-Review & Editing, Conceptualization. Dan Xiao: Methodology, Conceptualization. Mingxin Huo: Resources.

Acknowledgments

This work was funded by the National Natural Science Foundation of China (No. 51978135 and 51908062). It was also supported by the Scientific and Technological Development Plan Project of Changchun City (No. 21ZY30) and Jilin Province (No. 20200201042JC).

References

Abadie, T., al Ma Awali, S.M., Brennan, B., Briciu-Burghina, C., Tajparast, M., Passos, T.M., Durkan, J., Holland, L., Lawler, J., Nolan, K., Quilty, B., Fitzsimons, L., Regan, F., Delauré, Y., 2022. Oxygen transfer of microbubble clouds in aqueous solutions-Application to

wastewater. Chem. Eng. Sci. 257, 117693.

Agarwal, A., Ng, W.J., Liu, Y., 2011. Principle and applications of microbubble and nanobubble technology for water treatment. Chemosphere 84, 1175-1180.

Agarwal, A., Zhou, Y.F., Liu, Y., 2016. Remediation of oil-contaminated sand with self-collapsing air microbubbles. Environ. Sci. Pollut. R. 23, 23876-23883.

Alheshibri, M., Baroot, A.A., Shui, L., Zhang, M., 2021. Nanobubbles and nanoparticles. Curr. Opin. Colloid Interface Sci. 55, 101470.

Azevedo, A., Etchepare, R., Calgaroto, S., Rubio, J., 2016. Aqueous dispersions of nanobubbles: Generation, properties and features. Miner. Eng. 94, 29-37.

Barrio-Perotti, R., Blanco-Marigorta, E., Argüelles-Díaz, K., Fernández-Oro, J., 2009. Experimental evaluation of the drag coefficient of water rockets by a simple free-fall test. Eur. J. Phys. 30, 1039-1048.

Chang, T.J., Yen, B.C., 1998. Gravitational fall velocity of sphere in viscous fluid. J. Eng. Mech. 124, 1193-1199.

Chuang, T., Hibiki, T., 2017. Interfacial forces used in two-phase flow numerical simulation. Int. J. Heat Mass Tran. 113, 741-754.

Courtney, C., Brison, A., Randall, D.G., Calcium removal from stabilized human urine by air and CO2 bubbling. Water Res. 202, 117467.

Daitche, A., 2013. Advection of inertial particles in the presence of the history force: Higher order numerical schemes. J. Comput. Phys. 254, 93-106.

Darmana, D., Deen, N.G., Kuipers, J.A.M., Harteveld, W.K., Mudde, R.F., 2009. Numerical study of homogeneous bubbly flow: Influence of the inlet conditions to the hydrodynamic behavior. Int. J. Multiph. Flow 35, 1077-1099.

Duineveld, P.C., 1995. The rise velocity and shape of bubbles in pure water at high Reynolds-number. J. Fluid Mech. 292, 325-332.

Fan, W., Cui, J., Li, Q., Huo, Y., Xiao, D., Yang, X., Yu, H., Wang, C., Jarvis, P., Lyu, T., Huo, M., 2021. Bactericidal efficiency and photochemical mechanisms of micro/nano bubble-enhanced visible light photocatalytic water disinfection. Water Res. 203, 117531.

Feng, J.Y., Bolotnov, I.A., 2017. Interfacial force study on a single bubble in laminar and turbulent flows. Nucl. Eng. Des. 313, 345-360.

Ghadimkhani, A., Zhang, W., Marhaba, T., 2016. Ceramic membrane defouling (cleaning) by air Nano Bubbles. Chemosphere 146, 379-384.

Hirai, S., Aoki, S., Kohmura, M., 2015. Calculation method for change of micro-bubble diameter. Int. J. Inf. 18, 2589-2592.

ISO 20480-1:2017. Fine bubble technology-General principles for usage and measurement of fine bubbles-part 1: terminology. https://www.iso.org/obp/ui/#iso:std:iso:20480:-1:ed-1:v1:en.

Jadhav, A.J., Barigou, M., 2021. On the clustering of bulk nanobubbles and their colloidal stability. J. Colloid Interface Sci. 601, 816-824.

John, A., Carra, I., Jefferson, B., Jodkowska, M., Brookes, A., Jravis, P., 2022a. Are microbubbles magic or just small? A direct comparison of hydroxyl radical generation between microbubble and conventional bubble ozonation under typical operational conditions. Chem. Eng. J. 435, 134854.

John, A., Brookes, A., Carra, I., Jefferson, B., Jarvis, P., 2022b. Microbubbles and their application to ozonation in water treatment: a critical review exploring their benefit and future application, Crit. Rev. Environ. Sci. Technol. 52, 1561-1603.

Khuntia, S., Majumder, S.K., Ghosh, P., 2012. Microbubble-aided water and wastewater purification: a review. Rev. Chem. Eng. 28, 191-221.

Kulkarni, A.A., Joshi, J.B., 2005. Bubble formation and bubble rise velocity in gas-liquid systems: A review. Ind. Eng. Chem. Res. 44, 5873-5931.

Lee, J.I., Huh, H.S., Park, J.Y., Han, J., Kim, J., 2021. Coarsening behavior of bulk nanobubbles in water. Sci. Rep. 11, 19173.

Li, P., Takahashi, M., Chiba, K., 2009. Degradation of phenol by the collapse of microbubbles. Chemosphere 75, 1371-1375.

Liu, L., Yan, H., Zhao, G., Zhuang, J., 2016. Experimental studies on the terminal velocity of air bubbles in water and glycerol aqueous solution. Exp. Therm. Fluid Sci. 78, 254-265.

Liu, S., Li, J., Oshita, S., Kamruzzaman, M., Cui, M., Fan, W., 2021. Formation of a hydrogen radical in hydrogen nanobubble water and its effect on copper toxicity in chlorella. ACS Sustain. Chem. Eng. 9, 11100-11109.

Levitsky, I., Tavor, D., Gitis, V., 2022. Micro and nanobubbles in water and wastewater

631 treatment: A state-of-the-art review. J. Water Process. Eng. 47, 102688.
632 Lyu, T., Wu, S., Mortimer. R., Pan, G., 2019. Nanobubble technology in environmental
633 engineering: revolutionization potential and challenges, Environ. Sci. Technol. 53,
634 7175-7176.
635 Miner, E.W., Griffin, O.M., Skop, R.A., 1986. Near-Surface Bubble Motions in Sea Water. 1986.
636 Naval Research Laboratory, Washington, D. C. Page 5.
637 https://apps.dtic.mil/sti/citations/ADA168395.
638 Moreno-Casas, P.A., Bombardelli, F.A., 2016. Computation of the Basset force: recent
639 advances and environmental flow applications. Environ. Fluid Mech. 16, 193-208.
640 Muhlbauer, A., Hlawitschka, M.W., Bart, H.J., 2019. Models for the Numerical Simulation of
641 Bubble Columns: A Review. Chem. Ing. Tech. 91, 1747-1765.
642 Muroyama, K., Imai, K., Oka, Y., Hayashi, J., 2013. Mass transfer properties in a bubble
643 column associated with micro-bubble dispersions. Chem. Eng. Sci. 100, 464-473.
644 Nirmalkar, N., Pacek, W., Barigou, M., 2018. On the existence and stability of bulk
645 nanobubbles. Langmuir 34, 10964-10973.
646 Ohgaki, K., Khanh, N. Q., Joden, Y., Tsuji, A., Nakagawa, T., 2010. Physicochemical approach to
647 nanobubble solutions. Chem. Eng. Sci. 65, 1296-1300.
648 Parkinson, L., Sedev, R., Fornasiero, D., Ralston, J., 2008. The terminal rise velocity of 10-100
649 mu m diameter bubbles in water. J. Colloid Interf. Sci. 322, 168-172.
650 Parmar, R., Majumder, S. K., 2015. Terminal rise velocity, size distribution and stability of
651 microbubble suspension. Asia-Pac. J. Chem. Eng. 10, 450-465.
652 Pawliszak, P., Ulaganathan, V., Bradshaw-Hajek, B.H., Manica, R., Beattie, D.A., Krasowska, M.,
653 2019. Mobile or immobile? Rise velocity of air bubbles in high-purity water. J. Phys.
654 Chem. C 123, 15131-15138.
655 Plesset, M.S., Sadhal, S.S., 1982. On the stability of gas bubbles in liquid-gas solutions. Appl.
656 Sci. Res. 38, 133-141.
657 Seddon, J.R.T., Lohse, D., Ducker, W.A., Craig, V.S.J., 2012. A deliberation on nanobubbles at
658 surfaces and in bulk. Chemphyschem 13, 2179-2187.
659 Soyluoglu, M., Kim, D., Zaker, Y., Karanfil, T., 2021. Stability of oxygen nanobubbles under
660 freshwater conditions. Water Res. 206, 117749.

Sun, L., Zhang, F., Guo, X., Qiao, Z., Zhu, Y., Jin, N., Cui, Y., Yang, W., 2022. Research progress on bulk nanobubbles. Particuology 60, 99-106.

Takahashi, M., 2005. ζ potential of microbubbles in aqueous solutions: Electrical properties of the gas-water interface. J. Phys. Chem. B 109, 21858-21864.

Takahashi, M., Chiba, K., Li, P., 2007. Free-radical generation from collapsing microbubbles in the absence of a dynamic stimulus. J. Phys. Chem. B 111, 1343-1347.

Takahashi, M., Ishikawa, H., Asano, T., Horibe, H., 2012. Effect of microbubbles on ozonized water for photoresist removal. J. Phys. Chem. C 116, 12578-12583.

Tanaka, S., Kastens, S., Fujioka, S., Schlüter, M., Terasaka, K., 2020. Mass transfer from freely rising microbubbles in aqueous solutions of surfactant or salt. Chem. Eng. J. 387, 121246.

Tang, Y., Zhang, M., Zhang, J., Lyu, T., Cooper, M., Pan, G., 2021. Reducing arsenic toxicity using the interfacial oxygen nanobubble technology for sediment remediation. Water Res. 205, 117657.

Temesgen, T., Bui, T.T., Han, M., Kim, T.I., Park, H., 2017. Micro and nanobubble technologies as a new horizon for water-treatment techniques: A review. Adv. Colloid Interfac. 246, 40-51.

Terasaka, K., Hirabayashi, A., Nishino, T., Fujioka, S., Kobayashi, D., 2011. Development of microbubble aerator for waste water treatment using aerobic activated sludge. Chem. Eng. Sci. 66, 3172-3179.

Tsuchida, K., Maruyama, A., Kobayashi, Y., Sato, G., Atsumi, R., Murakami, Y., 2022. Influence of microbubble on free radical generation by ultrasound in aqueous solution: implication of the important roles of nanobubbles. Res. Chem. Intermed. 48, 1045-1061.

Xiao, Z., Aftab, T.B., Li, D., 2019. Applications of micro-nano bubble technology in environmental pollution control. Micro Nano Lett. 14, 782-787.

Xue, S., Zhang, Y., Marhaba, T., Zhang, W., 2022. Aeration and dissolution behavior of oxygen nanobubbles in water. J. Colloid Interface Sci. 609, 584-591.

Yasui, K., Tuziuti, T., Kanematsu, W., 2016. Extreme conditions in a dissolving air nanobubble. Phys. Rev. E 94, 13106-13106.

Yasui, K., Tuziuti, T., Kanematsu, W., 2018a. Mysteries of bulk nanobubbles (ultrafine bubbles):

691 stability and radical formation. Ultrason. Sonochem. 48, 259-266.
692 Yasui, K., Tuziuti, T., Kanematsu, W., 2018b. High temperature and pressure inside a
693 dissolving oxygen nanobubble. Ultrason. Sonochem. 55, 308-312.
694 Zhang, M, Qiu, L, Liu, G., 2020. Basic characteristics and application of micro-nano bubbles in
695 water treatment. 2020 IOP Conf. Ser.: Earth Environ. Sci. 510, 042050.
696 Zimmerman, W.B., Tesar, V., Bandulasena, H.C.H., 2011. Towards energy efficient nanobubble
697 generation with fluidic oscillation. Curr. Opin. Colloid Interface Sci. 16, 350-356.

Nomenclature

699	F_g	buoyancy force, N
700	F_b	gravity, N
701	F_d	drag force, N
702	F_A	virtual mass force, N
703	F_B	Basset force, N
704	m_g	mass of bubble, kg
705	u	bubble velocity, m/s
706	t	time, s
707	T	temperature, K
708	z	water depth, m
709	r	bubble radius, m
710	g	gravitational acceleration, m/s^2
711	C_D	bubble drag coefficient, dimensionless
712	Re	Reynolds number, dimensionless
713	Eo	Eötvös number, dimensionless
714	P	pressure inside bubble, Pa
715	P_0	ambient static pressure, Pa
716	R	universal gas constant, $Pa \cdot m^3/(mol \cdot K)$
717	W_i	mass transfer coefficient of gas species i, m/s
718	n_i	moles number of the gas species i inside a bubble, mol
719	n_t	total number of moles inside a bubble, mol
720	$n_{O_2,0}$	initial number of moles of oxygen inside the bubble, mol
721	$n_{O_2,t}$	number of moles of oxygen inside the bubble at the time *t*, mol
722	$C_{a,i}$	concentration of the gas species i in the surrounding ambient fluid, mol/m^3
723	$C_{s,i}$	concentration of the gas species i inside the bubble, mol/m^3
724	D_i	molecular diffusivity of the gas species i, m^2/s
725	$K_{H,i}$	Henry's law constant of the gas species i, Pa

726 r_i molar ratio of the gas species i in the surrounding ambient fluid, dimensionless

727 $r_{s,i}$ molar ratio of the gas species i inside the bubble, dimensionless

728 $M_{\mathrm{H_2O}}$ molecular weight of H_2O, kg/mol

729 j_{O_2} oxygen utilization coefficient, dimensionless

730 ρ_g gas density, kg/m^3

731 ρ_l liquid density, kg/m^3

732 τ dummy integration variable

733 σ surface tension of liquid, N/m

734 μ viscosity of liquid, N/m^2